Simulations of Magnetic Vortex Nucleation at Grain Boundaries in RF Superconducting Cavities

Jared Carlson

A senior thesis submitted to the faculty of
Brigham Young University
in partial fulfillment of the requirements for the degree of

Bachelor of Science

Mark Transtrum, Advisor

Department of Physics and Astronomy

Brigham Young University

ABSTRACT

Simulations of Magnetic Vortex Nucleation at Grain Boundaries in RF Superconducting Cavities

Jared Carlson
Department of Physics and Astronomy, BYU
Bachelor of Science

Superconducting Radio Frequency (SRF) cavities are important components of particle accelerators. SRF cavity performance is limited by a maximum allowed applied magnetic field, known as the superheating field (H_{sh}) at which magnetic vortices spontaneously enter the material and cause the superconducting material to quench. Previous work has calculated the theoretical maximum field a superconductor can withstand. However, this calculation assumed a perfectly smooth surface with no material inhomogeneities or surface roughness. Real world cavities are polycrystalline (typically Nb or Nb_3Sn) and exhibit surface defects near grain boundaries. Cavity preparation methods also lead to material inhomogeneities. I use the time-dependent Ginzburg-Landau theory and finite element methods to model the role of surface defects and material inhomogeneities in magnetic vortex nucleation. Results show the amount by which Hsh is reduced depends on the concentration of impurities as well as the physical dimensions of the defect. Reducing the size of grain boundaries and material inhomogeneities found therein has the potential to significantly increase SRF cavity performance.

Keywords: Superconductor, Superheating Field, Inhomogeneities, Grain Boundary, Computation, Simulation, SRF Cavities

ACKNOWLEDGMENTS

To my ever supportive and loving wife, Christina. My mother, Dave Jenks, and Kyle McEuen for being mentors and supports to me. To my friend Adam Finder for helping me stay in school. To my family members and friends for their support.

To my advisor Mark Transtrum and colleague Alden Pack for their instruction, guidance, and patience in helping me conduct this research. To Professors Justin Peatross, Branton Campbell, and John Colton for helping me excel in my upper division coursework while at Brigham Young University. To Traci Neilsen for providing in-depth feedback on each draft of this thesis.

To Professors Michael Santilli, Stacy Wilson, Eric Menu and Tara Jones for instilling in me a desire for excellence and dedication during my time at Mesa Community College.

Contents

List of Figures

Chapter 1

Introduction

1.1 Motivation

Many particle accelerators transfer energy to charged particles though large oscillating electric fields in superconducting radio frequency (SRF) cavities. This involves driving large currents through the superconducting cavities, whose geometry aids in amplifying these fields. These currents occur on the interior of the cavities where the superconducting material is present. In most SRF cavities the superconducting material used is Nb, but Nb_3Sn is also being explored as a possible candidate. As particles pass through these cavities, they gain forward momentum from the electric field. The oscillations are timed such that for each pass by the particle it is accelerated in the same direction. The main source of power loss in these cavities comes from the ac resistance, and the power needed to keep the cavities cooled to $\sim$10 K [1].

The limiting component in SRF cavities is the superconductor, which loses its superconductivity when exposed to high magnetic (H) fields. This effect, which is addressed more in Sec. 1.2, increases the resistance of the cavity, which increases the heat loss. In SRF cavities, H fields form due to the oscillating electric field. Thus the limitation of a maximum H field imposes a limitation

on the maximum electric field, which therefore limits the effectiveness of the cavity. The maximum H field above which the superconductor begins to lose some of its superconductivity is called the superheating field (H_{sh}) and is discussed in Sec. 1.5. Our research seeks to understand the mechanism of this limitation so that more effective SRF cavities can be made [2].

1.2 Superconductors

Magnetic fields are normally expelled from superconductors due to the Meissner effect. This effect occurs when a material is cooled to below its superconducting temperature, at which point the H field is expelled from the superconductor. This expulsion process and the resulting possibility of trapped pockets of magnetic flux within a superconductor after it has been cooled, is an active area of study [3]. Once the material is in a superconducting state, applied H fields are kept out by screening currents, which form on the surface of the material. These currents, also called persistent currents, continue to exist with no resistance due to the superconducting state of the material. The end effect is an exponential decay of the H field from its value at the surface to zero as it enters into the superconductor. The length at which the magnetic field has decayed to $1/e$ its original value defines the characteristic length, which is called the London penetration depth (λ).

At high applied H fields, quantized pockets of H fields, called vortices, can push into the superconductor, causing the portion of metal they occupy to lose its superconducting properties. This processes is called vortex nucleation and is a distinguishing characteristic of Type-II superconductors. In Type-I superconductors, this transition from superconducting to non-superconducting involves a bulk change (the magnetic field pushes in all at once) instead of the formation of vortices [4]. Our research focuses on Type-II superconductors.

In Type-II superconductors, there are four states that a superconductor can exist in, the boundary of each being characterized by an applied magnetic field, see Fig. 1.1. The first state is the

superconducting state, where the entire bulk is superconducting. At higher applied fields the next state is the meta-stable state. In the meta stable state, it is energetically favorable for vortices to exist within the superconductor but there is not enough energy for them to enter. This is analogous to superheated water; it is hot enough to boil, but the surface tension keeps it from doing so. This meta-stable state is where most accelerator cavities operate. H_{c1} is the boundary between the superconducting state and a meta stable state. The next state is the mixed state, where vortices enter into and fill the bulk. The vortices repel each other and create an array, leaving the space in between them superconducting. The boundary between the meta-stable and mixed state is called the superheating field H_{sh}, which is dependent on the material, its surface features, and purity. The final state is the normal metal state, where the magnetic field completely fills the bulk and there is no longer any superconducting regions remaining. The transition between the mixed and normal metal state is called H_{c2}. Because cavities are operated in the meta stable state, it is important to know how to increase H_{sh} so that higher H fields can be reached without entering the mixed state, which is undesirable.

1.3 Grain Boundaries

Grain boundaries—which are defects in the interface between two grains in a material, see Fig. 1.2—are thought to be a major contributing factor to the lowering of H_{sh} in real superconductors. One of the materials being investigated as a replacement for Nb (niobium) as the material used in SRF cavities is Nb_3Sn, which the theory predicts to have a higher H_{sh} than Nb [2]. Efforts to reach this theoretical maximum, however, have come up short. Grain boundaries are suspected to be the culprit to the lowering of H_{sh} [5] [6]. A picture of such a grain boundary is shown in Fig. 1.2. This research seeks to understand how grain boundaries affect H_{sh}.

Grain boundaries can also be sources of material inhomogeneities. An example of this is shown

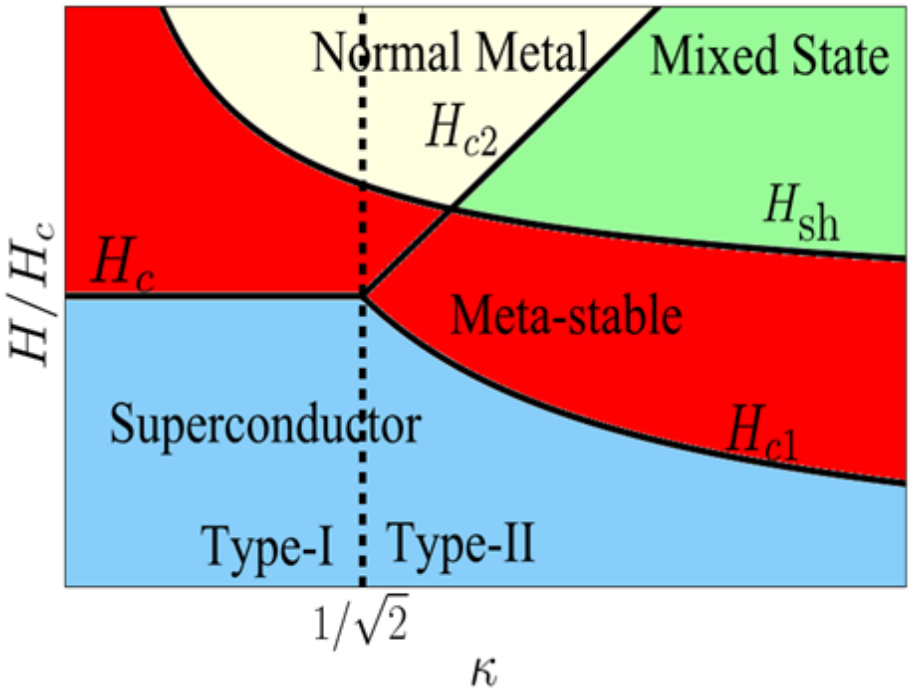

Figure 1.1 A phase diagram showing the states of a superconductor. H is the magnetic field, H_c is the critical H field at which Type-I superconductors transition into normal metals, H_{c1} and H_{c2} are the lowers and upper bounds for phase transition of Type-II superconductors, and H_{sh} is when vortices begin to enter. κ is a material dependent superconducting parameter.

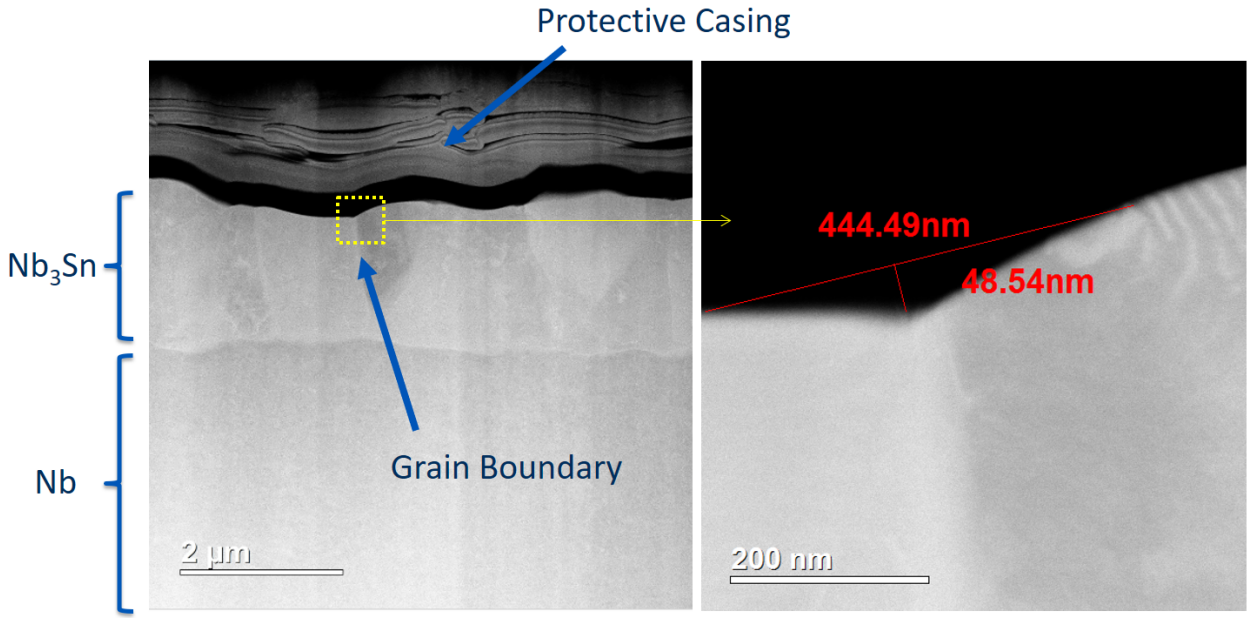

Figure 1.2 A image of a grain boundary found in Nb_3Sn deposited on a layer of Nb. The black gap above the Nb_3Sn is free space with a protective casing above that. Images courtesy of Jaeyel Lee at Cornell University.

in Fig. 1.3, where excess Sn (Tin), or Sn segregation, has been found at grain boundaries. The implications of this are that Sn has different superconducting properties than Nb_3Sn and thus can change the maximum H field that can be present at these locations before vortices begin to enter [2].

1.4 Modeling Superconductors

The superconducting properties of a metal can be modeled using the Ginzburg-Landau equations. These equations come from a Taylor approximation of the Helmholtz free energy of a superconductor. The derivation and resulting equation, shown in Eq. (1.1), are found in Introduction to Superconductivity by Michael Tinkham. By minimizing the free energy of the superconductor, equations that model the superconductivity of a material, called the Ginzburg-Landau equations (1.2) [7], are obtained:

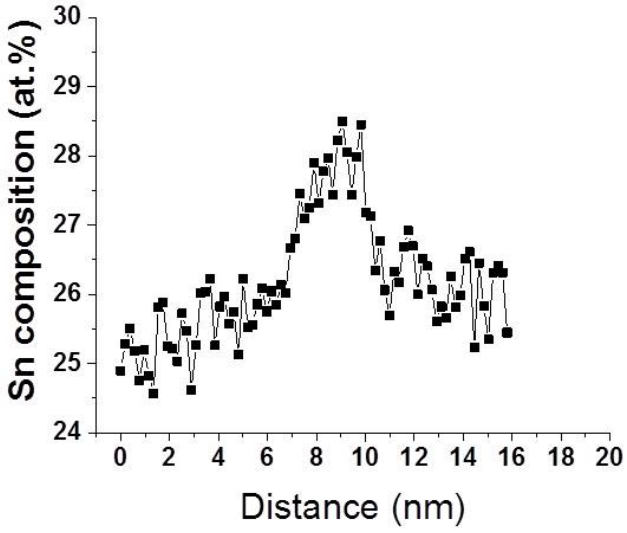

Figure 1.3 An image of Sn segregation across Nb_3Sn grain boundary. This is scanning perpendicular to the grain boundary and was provided by of Jaeyel Lee at Cornell University.

$$F = f_n + \alpha \mid \psi \mid^2 + \frac{\beta}{2} \mid \psi \mid^4 + \frac{1}{2m} \mid (-i\hbar\nabla - 2e\mathbf{A})\psi \mid^2 + \frac{\mid \mathbf{H} \mid^2}{2\mu_0} \tag{1.1}$$

$$\begin{aligned} 0 &= \alpha\psi + \beta \mid \psi \mid^2 \psi + \frac{1}{2m}(-i\hbar\nabla - 2e\mathbf{A})^2\psi \\ \mathbf{j} &= \frac{2e}{m} Re\{\psi^*(-i\hbar\nabla - 2e\mathbf{A})\psi\} \end{aligned} \tag{1.2}$$

An important component in these equations is ψ, the complex order parameter. An order parameter describes a phase transition, *e.g.*, water evaporating into steam. In this case, it is the phase transition from non-superconducting to superconducting. When $\mid \psi \mid^2 = 1$ the material is completely superconducting, and when $\mid \psi \mid^2 = 0$ the material is a normal metal. As seen in equations 1.1-1.2, the solution to ψ is dependent on the magnetic field and potential (**H** and **A**), and other parameters. One of these parameters, α, represents specific material proprieties and is discussed in Sec. 2.4. When vortices enter into a material, the order parameter becomes zero within the vortex, which size

is related to two length scales, ξ and λ.

The relative length scales to consider in vortex penetration are the penetration depth (λ) and coherence length (ξ). The coherence length (ξ) is the characteristic length over which variation in the superconducting order parameter $\mid \psi \mid^2$ can vary without undue variations in the free energy of the superconductor. The penetration depth (λ) is the characteristic length over which H dies off in a superconductor. Thus for a vortex that has penetrated into a superconductor, the vortex has a radius of ξ over which it destroys superconductivity and a radius of λ over which the magnetic field is spilling over into the superconductor [2]. These value of λ and ξ are material dependent.

The ratio of the two length scales of λ and ξ is known as the Ginzburg-Landau parameter $\kappa = \frac{\lambda}{\xi}$. As discussed in Sec. 1.2, κ distinguishes between Type-I and Type-II superconductors. The dividing line is at $\kappa = \frac{1}{\sqrt{2}}$, with Type-II superconductors having a κ above this value. For our simulations, we set $\lambda = 1$ and adjust κ to simulate different materials.

1.5 The Superheating Field (H_{sh})

The superheating field (H_{sh}) is the maximum magnetic field (H) that can be applied before vortices begin to enter into a Type-II superconductor with or without geometric and material inhomogeneities. This is slightly different from other definitions in that it includes defects in materials, whereas other definitions rely on purely theoretical ideal cases [2].

Theoretical results for an ideal case predict a higher H_{sh} than found experimentally [2]. One of the goals of our research is to see if defects and material inhomogeneities are the cause of this divergence of experimental results from theoretical predictions.

Grain boundaries are suspected to be the cause of the discrepancy between experimental and theoretical H_{sh} predictions. Theoretical calculations of H_{sh} use a perfect superconductor occupying a half space (3D space with free space in -x and superconductor in +x). These results predict a

higher H_{sh} than found experimentally. One theory attributes this to vortex penetration at grain boundaries, which have a curved geometry and Sn segregation, as shown in Figs. 1.2 and 1.3. To measure the effects of grain boundaries on H_{sh}, we computationally estimate H_{sh} for geometries similar to those observed in real grain boundaries [2].

To computationally estimate H_{sh}, we start by solving the Ginzburg-Landau (GL) equations (Eq. 1.2) using finite element methods for a given applied field. After stepping through time until the dynamics of the systems approach equilibrium, we add noise and calculate the decay rate of $|\psi|^2$ back to the steady state. This process is repeated for many applied fields to estimate the H_{sh}. A more in-depth explanation of this is given in Sec. 2.6.

1.6 Overview

The purpose of this research is to explore the effects grain boundaries have on superconducting properties. This work is motivated by the need for more efficient SRF cavities in particle accelerators. The limiting factor in these cavities is the maximum magnetic field (H_{sh}) that can be present before the superconducting material loses its superconducting properties. This magnetic field is produced by a large oscillating electric field within the cavity. Grain boundaries in the superconducting material are suspected to lower H_{sh}.

In Ch.2, an explanation of the numerical methods used to model grain boundaries and calculate their H_{sh} is given. We do this by explaining the formulation of the Ginzburg-Landau equations and how we use finite element methods to solve them. A case where there are no grain boundaries is examined and compared to previous theoretical work. Then the formation of vortices in cases where surface defects and material inhomogeneities are present is verified. Our methods used to calculate H_{sh} are then explained.

In Ch.3, we present the results of our calculated values H_{sh} for three different configurations:

symmetric, surface roughness and material inhomogeneities. Our results show that both material inhomogeneities and surface roughness influence H_{sh}. We conclude with an analysis of our results and a discussion on future work and limitations.

Chapter 2

Numerical Methods

To better understand the effects of grain boundaries on H_{sh}, I develop simulations modeling the geometry and material inhomogeneities present at grain boundaries. First, the problem is formulated such that finite element methods can be used. Next, I confirm the theoretical estimation for an ideal symmetric case and describe how grain boundary geometries and inhomogeneities are introduced into the simulation. This chapter concludes with a brief description of saddle node bifurcations and how H_{sh} is estimated. Results from the exploration of the relevant parameter space due to material inhomogeneities and grain boundary geometries are presented in Ch.3.

2.1 Solving the Ginzburg-Landau Equations

To simulate a superconductor I use the formulation of the Ginzburg-Landau time dependent equations as given by Buyang and Zhang [8]. Using these formulations, a finite element solver was created using FEniCS. The derivation of this formulation is beyond the scope of this thesis but is presented in the cited paper.

The Ginzburg-Landau (GL) equations are solved using finite element methods. The GL equations are coupled partial differential equations that describe the superconductivity of a material over

a domain, given initial and boundary conditions. Two important variables in this formulation are the order parameter ($|\psi|^2$) and the applied magnetic field (H). The boundary conditions fix H, while the order parameter $|\psi|^2$—a measure of the superconductivity of the material—is the main observable. The domain over which the problem is solved is discretized using finite element methods: Each point is connected to other points creating a mesh of points.

In our problem, each point has a series of scalar variables, which are solved for such that they best approximate the solution the GL equations over the domain of the mesh. Vector quantities, such as the magnetic potential, are broken into multiple scalar variables. Because the GL equations are time dependent, the solution of the variables over the mesh is dependent on their previous values.

In solving the GL equations, the ideal situation is to look at the dynamics of the solution for an infinite half plane with an H field applied to one side, perpendicular to our 2D representation. This is a good representation of the exterior of an SRF cavity, as the curvature of the cavity is much larger than any length scale that contributes to the dynamics of our simulation. Due to finite computational resources, a circular mesh is used which, in the limit that length scales are small compared to the curvature of the mesh, approximates an infinite plane.

The mesh's construction is based on the point density needed to capture the dynamics of the system and the geometry of the surface roughness. The density at the boundary of the mesh also needs to be dense enough to capture the curvature of the disk. Along with the geometry, the mesh must be fine enough that the dynamics of interest, e.g., vortex penetration, can be accurately captured. If distances between mesh points are greater than the size of a vortex, the vortex might disappear if it enters one of these regions. Because refining the mesh increases the computational resources needed, I refine the boundary more than the interior, because the boundary is where the most important dynamics happen.

FEniCS acts as our finite element solver. FEniCS is an open source solver that uses C/C++ at its core to compute the solutions and has a Python interface. The Python interface allows for rapid

prototyping and development while having a C/C++ core allows for fast computations.

2.2 Symmetric Case

The simulation of a perfectly smooth and homogeneous SC cavity begins with approximating it as a smooth half space, which can then be approximated as a disk. Mesh generation is done by creating concentric circles of points, as shown in Fig. 2.3a. The circle locations are biased outwards to give more refinement at the boundary. The points are then aligned in such a way that they are symmetric with the previous and next layer of points. This symmetry increases the accuracy of the solutions.

As a first step in calculating H_{sh}, a magnetic field (H) is applied uniformly throughout the mesh through an exponentially increasing function, shown in Fig. 2.2. This function starts at zero and asymptotically approaches a desired applied field. Due to the Meissner effect, as the applied field is increased screening currents begin to form near the surface that keeps the magnetic field within the superconductor zero. If the field exceeds H_{sh}, vortices begin to enter into the bulk.

As the first step in verification of our simulations, I verify that vortices penetrate in a uniform array above the H_{sh}, as predicted by theory [2]. By raising H above the known value of the H_{sh} and evolving the system, we observe vortex penetration into the bulk as seen in Fig. 2.3b. This figure shows the order parameter squared, $\mid \psi \mid^2$, which is a measure of the superconductivity of the material ($\mid \psi \mid^2 = 1$ being fully superconducting), over the mesh. At the start, $\mid \psi \mid^2$ it is one everywhere. Once the applied field is raised, vortices begin to penetrate in a regular array into the interior of the mesh. If more time were allowed to elapse, the bulk would fill with vortices. As expected, the value of $\mid \psi \mid^2$ at the center of a vortex is zero, with $\mid \psi \mid^2$ exponentially increasing radially from the vortex's center to one, with ξ, the coherence length, being the characteristic length of decay, i.e. when $\mid \psi \mid^2$ has decay back to $1/e$ of its original value, in this case being $\mid \psi \mid^2 = 1$.

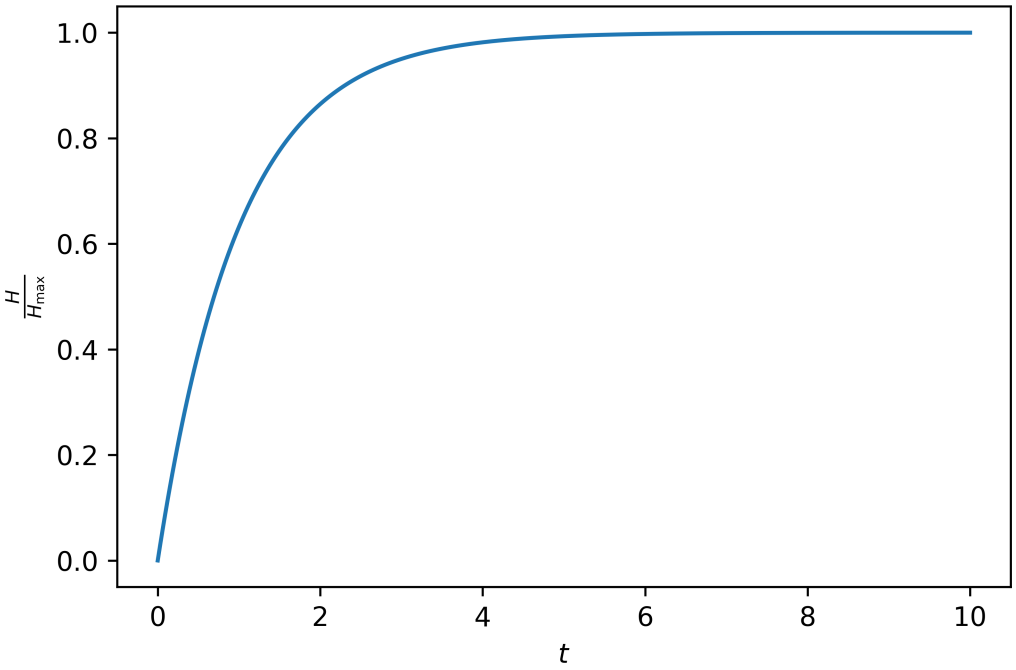

Figure 2.1 Profile of Applied Field

Figure 2.2 The applied magnetic field H exponentially decays to its max value $H_{\max}$.

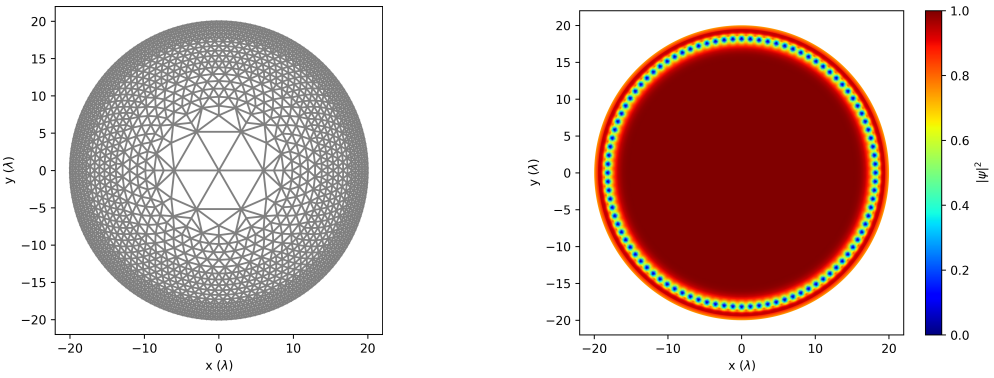

(a) Symmetric mesh **(b)** Vortex formation

Figure 2.3 (a) Symmetric mesh over which the Ginzburg-Landau equations are solved. (b) Formation of vortices when a magnetic field, H, is applied that is greater than the superheating field, H_{sh}, on a symmetric mesh with no material inhomogeneities.

2.3 Introducing Grain Boundary Geometries

To add realism to the model, a mesh is generated to replicate the geometry of a grain boundary on the surface, with increased refinement along the regions of higher curvature. The mesh is generated by defining concentric regions, each with its own density of points. The boundaries of these regions are curved such that they have the form of a grain boundary, see Fig. 1.2. This adaptation allows radial control of the mesh's refinement.

The first step in generating the mesh is to create the domains. Domains are defined by first creating a list of points that make up a ring. The points are equal distances along a curve defined by

$$r(\theta) = R - B\exp\left(\frac{-\mid \theta R \mid}{2\sigma}\right), \tag{2.1}$$

where R is the radius of the ring, B is the depth of the grain boundary, θ is the angle from the y-axis, and σ is the half width of the grain boundary. The domain is defined as the region between this ring and the next interior ring, or the center of the disk if it is the innermost ring. Depending on the different levels of desired density, rings are made such that each region corresponds to an area of desired density, e.g., two rings close together at the boundary and one halfway to the center would allow for high density at the surface, medium density in the outer half, and low density in the center.

To increase the accuracy of the simulations, I create meshes with a high density of points on the boundary and decrease density towards the center, as seen in Fig. 2.4a. Creating high density at the boundary accurately captures the dynamics of vortex penetration and other dynamics important to calculating H_{sh}—discussed in Sec. 2.6—that happens near the outer boundary. I validate our hypothesis that grain boundaries contribute to H_{sh} by raising the applied magnetic field above H_{sh} and observe initial vortex penetration at the grain boundary before other places on the mesh, as seen in Fig. 2.4b.

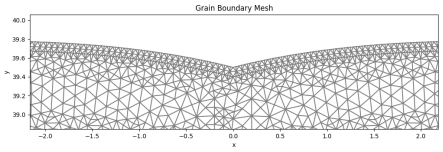

(a) Grain boundary mesh

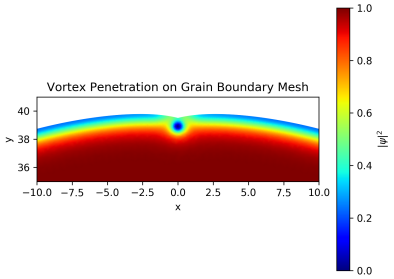

(b) Vortex formation

Figure 2.4 (a) A mesh with a geometry matching a grain boundary. (b) The order parameter, $|\psi|^2$, shows that vortices first begin to enter in at the grain boundary when $H > H_{sh}$. At the center of a vortex $|\psi|^2 = 0$, which then exponentially decays back to one radially from the vortex's center.

2.4 Introducing Material Inhomogeneities

To introduce material inhomogeneities into our simulations, I reformulate the Ginzburg-Landau equations to include a spatially dependent variable α, which represents the superconductivity of the composition (the superconductor plus inhomogeneities). A value of $\alpha = 1$ corresponds to no inhomogeneities, $\alpha = 0$ correspond to the composition acting like a normal metal. This formulation follows the approach of Tinkham (Eq. 4.13) [4], with all the same variable definitions. I start with the traditional GL equations Eqs. 2.2 and add in a spatial varying component to α and β.

$$\alpha\psi + \beta|\psi|^2\psi + \frac{1}{2m^*}\left(\frac{\hbar}{i}\nabla - \frac{e^*}{c}\mathbf{A}\right)^2\psi = 0 \tag{2.2}$$

$$\alpha_0\alpha(r)\psi + \beta_0 b(r)|\psi|^2\psi + \frac{1}{2m^*}\left(\frac{\hbar}{i}\nabla - \frac{e^*}{c}\mathbf{A}\right)^2\psi = 0. \tag{2.3}$$

Following the same process as Tinkham, I arrive at the same non-dimensionalized equations as Tinkham, only there are now two spatially dependent terms, $\alpha(r)$ and $b(r)$, see Eq. 2.4. Because β is approximately constant, I set $b(r) = 1$, leaving one spatially dependent parameter, $\alpha(r)$, which I use to model the inhomogeneities present at grain boundaries. The same procedure can be done for

equation (4.14) in Ref. [4].

$$\alpha(r)f + b(r)f^3 + \frac{1}{2m^*\alpha_0}\left(\frac{\hbar}{i}\nabla - \frac{e^*}{c}\mathbf{Q}\sqrt{2}\lambda H_c\right)^2 f = 0. \tag{2.4}$$

With a material dependent term (α) introduced, the profile of α is chosen to resemble the inhomogeneities in a grain boundary—an example of the inhomogeneities along a grain in Nb3Sn is shown in Fig. 1.3. Namely,

$$\alpha(\vec{r}) = A - B\exp\left(-\frac{(\theta R)^2}{2\sigma^2},\right) \tag{2.5}$$

where A is the upper limit of α, which is set to one, B is the lower limit of α, θ is the angle from the y-axis, R is the radius of the mesh, and σ is the characteristic half width of α. A configuration for α over a symmetric mesh is shown in Fig. 2.5a. In the limit that our curvature is larger than relevant length scales, the profile of α mimics the inhomogeneities observed in grain boundaries as seen from the surface, as shown in Fig. 1.3. To confirm that inhomogeneities are responsible for lower $H_{\rm sh}$, I verify that vortex penetration happen where material inhomogeneities are present ($\alpha < 1$) at an applied magnetic field lower than $H_{\rm sh}$ for the same mesh with no material inhomogeneities present, shown in Fig. 2.5b.

2.5 Saddle Node Bifurcations

One of our major results is the estimation of $H_{\rm sh}$, which is done by treating the transition of the superconductor from a meta stable state to a mixed state as a saddle node bifurcation. In this section, I briefly explain what it means for our system to be a saddle node bifurcation by using a made-up system, $f(x)$, shown in Fig. 2.6.

The shape of $f(x)$ depends upon a bifurcation parameter r (which is different from the r in Eq. 2.1), which is an adjustable parameter. Given a starting position in x space, the system tends towards

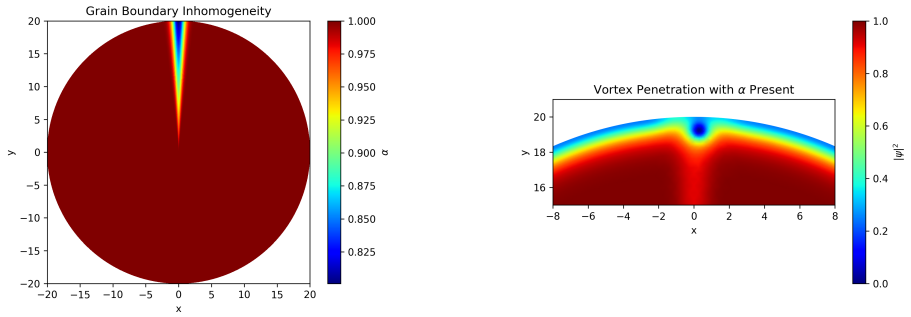

(a) Value of α **(b)** Vortex formation

Figure 2.5 (a) The material inhomogeneities, α, varied over a symmetric mesh simulating the material inhomogeneites at a grain boundary. $\alpha < 1$ correspond to material inhomogenieties. (b) The order parameter, $\mid \psi \mid^2$, shows vortex penetration for the same mesh and α configuration shown in (a). The vortex penetration happens where $\alpha < 1$ for an applied magnetic field less then H_{sh} for the same mesh without material inhomogeneities present, as shown in Fig 2.3b.

the local minimum of $f(x)$—picture the path of a ball rolling down the curves. The system also experience damping, so it eventually comes to rest at the minimum—imagine the ball experiences friction.

For low r, there are two minima and one maximum. As the bifurcation parameter r is increased, $f(x)$ changes form, as shown in Fig. 2.6a-2.6c. As r changes, one of the minima of $f(x)$ is annihilated by a maximum of $f(x)$, leaving just one minimum.

If the system starts with a low r value and at the minimum to the right in Fig. 2.6a and is perturbed, imagine giving the ball some energy; it oscillates around the minimum until dissipative factors bring it back to the minimum. This decay back to the minimum follows an exponential decay, with a characteristic decay rate of τ. As r increase and changes states form Fig. 2.6a to 2.6b, τ increases. At the critical value of r, Fig. 2.6b, the minimum and maximum annihilate each other, and the slope is zero where the minimum was. With a slope of zero, τ would be infinite, as the system would never return to the minimum. After r has changed past the critical value, the system always tends towards the left minimum, shown in Fig. 2.6c.

This system is analogous to Type-II superconductors, where r is some parameter that is dependent on the applied field. While the applied field is below some critical value, H_{sh}, a meta stable state exists, analogous to Fig. 2.6a: The left minimum is where vortices fill the bulk, and the right minimum is where no vortices exist. If the superconductor starts in a superconducting state and the applied field is raised, the system settles into the right minimum. If we perturb the system enough, vortices begin to form, and the system moves to the left minimum.

The field at which r is at its critical point is H_{sh}, for $H > H_{sh}$ the system tends to a state where vortices exist within the bulk. By perturbing the system from its local minimum and calculating the decay rates, we can find the r value that corresponds to a given applied field. A detailed explanation of why this is a saddle node bifurcation can be found in Alden Pack's Masters Thesis [9].

2.6 Calculating the Superheating Field (H_{sh})

The superheating transition is a saddle node bifurcation, where the bifurcation parameter, r, is dependent on the applied magnetic field (H). Thus, methods in bifurcation theory are used to estimate the superheating field, H_{sh}, where r$=0$. Using these methods, calculations are done for $H < H_{sh}$, where the dynamics, and therefore calculations, are faster. H_{sh} is then extrapolated from those results.

The superheating field is calculated computationally by first solving the time dependent Ginzburg-Landau (GL) equations over a mesh of points using finite element methods. The output is the solution to the equations after a given time step at all the points in the mesh. Using this method, the simulation iterates long enough for system dynamics to emerge and reach a steady state. Convergence to a steady state is measured using the tolerance

$$\max\left(\frac{|\psi_t|^2 - |\psi_{t-1}|^2}{\mathrm{dt}}\right) < 10^{-8}, \tag{2.6}$$

where dt is the time step.

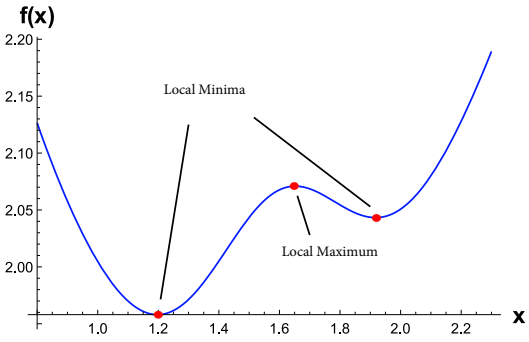

(a) System before critical point.

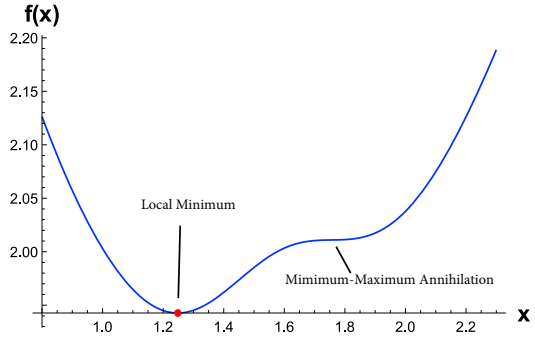

(b) System at critical point.

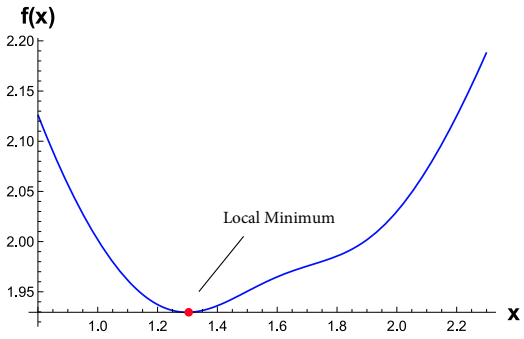

(c) System after critical point.

Figure 2.6 Different stages in a saddle node bifurcation. The transition from having two stable points and one unstable point (a) to one stable point (c) happens at the critical value of the bifurcation parameter r (b).

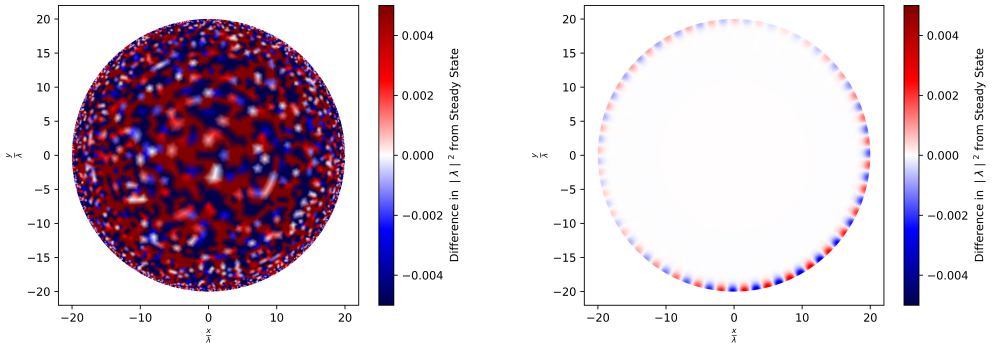

(a) **(b)**

Figure 2.7 (a) Difference in $|\psi|^2$ over mesh after white noise has been added to the steady state solution. (b) Lowest decaying mode remains after amplification processes has been completed.

To estimate H_{sh}, a system with a given H at steady state is perturbed by adding white noise, with the decay back to a steady state being measured. The noise is added to the order parameter, $|\psi|^2$, and a magnetic potential component, which is described later, at each element in the mesh. A plot of the difference from steady state to the state right after the noise is added is shown in Fig. 2.7a. Once the noise is added, the dynamics of the system tend back towards the steady state previously reached. The process of perturbing the system and calculating the decay rate is analogous to the processes of calculating τ in Sec. 2.5 where the system starts in the minima to the right in Fig. 2.6a.

After noise is introduced, an amplification process is used to pull out the lowest decaying modes. A mode is an oscillation in the difference in $|\psi|^2$ from steady state. All modes that can exist are present when white noise is introduced. An example of a mode is shown in Fig. 2.7b. As the system decays back into a steady state, different modes decay at different rates. The lowest decaying mode can be related back to the bifurcation parameter r and, thus, is of interest. To isolate this mode, a process of amplification is used where the difference in $|\psi|^2$ from the current values to the steady state values are amplified by some given factor. In order to keep the solution stable, the angle between the imaginary and real parts of ψ are constrained to be constant during the amplification

processes. This amplification processes—re-amplifying when the solution gets close to steady state—is used until only one dominate mode remains, as shown in Fig. 2.7b.

The amplification problem is formulated as follows. Start with the steady state solution for ψ, which has both real and imaginary parts:

$$\psi_0(r) = a_0(r) + ib_0(r). \tag{2.7}$$

The r dependence is dropped from this point on. The equations for ψ before and after amplification are

$$\psi_1 = (a_1) + i(b_1) \tag{2.8}$$

$$\psi_a = (a_0 + \phi) + i(b_0 + \gamma), \tag{2.9}$$

respectively. The constraint that the complex angle must be constant through the amplification process requires

$$\frac{b_1}{a_1} = \frac{b_0 + \gamma}{a_0 + \phi}. \tag{2.10}$$

The desired change in $|\psi|^2$ is given by

$$\Delta|\psi_a|^2 = A(|\psi_1|^2 - |\psi_0|^2), \tag{2.11}$$

which is calculated numerically. This desired change can also be expressed in terms of ψ_a and ψ_0,

$$\Delta|\psi_a|^2 = |\psi_a|^2 - |\psi_0|^2 = (a_0 + \phi)^2 + (b_0 + \gamma)^2 - (a_0 + b_0)^2. \tag{2.12}$$

Using all these equations, ϕ and γ are solved for to get

$$\phi = -a_0 + a_1 \frac{\sqrt{(a_1^2+b_1^2)(a_0^2+b_0^2+\Delta|\psi_a|^2)}}{a_1^2+b_1^2} \tag{2.13}$$

$$= -a_0 + a_1 \frac{\sqrt{|\psi_1|^2(|\psi_0|^2+\Delta|\psi_a|^2)}}{|\psi_1|^2} \tag{2.14}$$

$$\gamma = -b_0 + b_1 \frac{\sqrt{(a_1^2+b_1^2)(a_0^2+b_0^2+\Delta|\psi_a|^2)}}{a_1^2+b_1^2} \tag{2.15}$$

$$= -b_0 + b_1 \frac{\sqrt{|\psi_1|^2(|\psi_0|^2+\Delta|\psi_a|^2)}}{|\psi_1|^2}. \tag{2.16}$$

With these expressions, Eq. 2.9 is used to calculate a new solution to ψ. The other variable that is amplified is a component of the magnetic field, u, which formulation was done by Buyang Li [8], and is defined by

$$\mathbf{A} = \nabla \times u + \nabla v, \tag{2.17}$$

$$-\Delta u = \nabla \times \mathbf{A} \text{ in } \Omega, \tag{2.18}$$

$$u = 0 \text{ on } \partial\Omega. \tag{2.19}$$

The u value is amplified via

$$u_a = A(u_1 - u_0), \tag{2.20}$$

where the same naming convention is used as with ψ.

To calculate the decay rate, a decaying exponential function is fitted to the decay of $|\psi|^2$ to its steady state values at all points on the mesh after the last amplification. The fit is formulated as the solution to

$$\Delta\psi(x,t) = M(x)e^{-\frac{t-t_0}{\tau}}, \tag{2.21}$$

where $M(x)$ is the unknown mode, and τ is the decay rate of the mode. To solve for τ, we formulate

this as a least squares problem,

$$\begin{pmatrix} \Delta\psi_i(t_0)^2 \\ \vdots \\ \Delta\psi_i(t_n)^2 \end{pmatrix} = \begin{pmatrix} e^{-\frac{t_0-t_0}{\tau}} \\ \vdots \\ e^{-\frac{t_n-t_0}{\tau}} \end{pmatrix} M_i \tag{2.22}$$

$$Y = TM_i, \tag{2.23}$$

where τ is supplied, i is the vertex index, n is the time step index, t is the time, and M is some unknown mode. With the value of τ initially given, the solution to Eq. 2.21 is $M_i = (T'T)^{-1}T'Y$. This formulation equates to a least squares projection, using the L2 norm, onto a function space of a decaying exponential. Using the residual of the fit, i.e, the distance our projected value is from the actual value, τ is adjusted to until a minimum is found in the residual error. The τ that produces the lowest residual is used [9]. From τ we calculate the bifurcation parameter:

$$r = \frac{1}{4\tau^2}. \tag{2.24}$$

To estimate H_{sh}, the r values that are close to H_{sh} are used to do a linear extrapolation. Only values close to H_{sh} are used in the extrapolation because of the linear relations, as shown in Fig. 2.8, which fits with our model of slightly perturbing the system. Values farther away from H_{sh} are included in this figure to illustrate the divergence from a linear relation. The extrapolation is based on those values that are within the linear regime. The calculated H_{sh}, in this case, is for a homogeneous symmetric case, which agrees with the theoretical predictions [10].

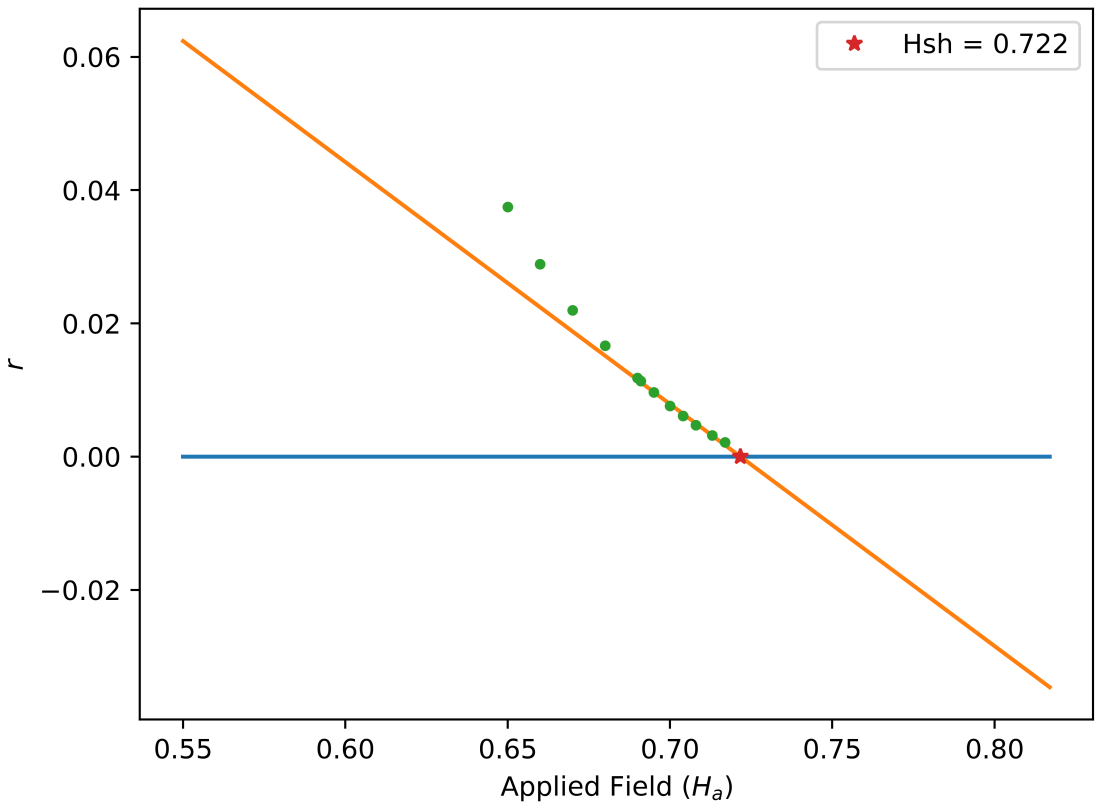

Figure 2.8 H_{sh} (red start) is estimated by extrapolating the applied magnetic field, H_a, that causes r to be zero. Only value close to r= 0 are considered. Points farther away are plotted to show the non-linear regime that exists when H_a is not close to H_{sh}.

Chapter 3

Results and Conclusions

3.1 Results

Using my simulations, estimates for the superheating field for a variety of cases are calculated: a symmetric mesh with no material inhomogeneities, a mesh modeling a grain boundary geometry with no material inhomogeneities, and a symmetric mesh with material inhomogeneities. By probing the parameter space in the latter two cases we show the behavior of H_{sh} for different possible types of grain boundaries.

The results from the symmetric case match with the theoretical prediction made for a superconductor occupying a half space, up to three significant figures [10]. With $\kappa = 4$, our results match that of theory with $H_{\mathrm{sh}} = 0.722$. We use this result as a baseline to compare the other cases, *i.e.* results for the non-ideal cases are expressed as a fractional decrease from this result. Thus our simulations are accurate for known cases.

The estimated values of H_{sh} when mesh geometries match that of a grain boundary show a significant decrease in H_{sh}. Because the grain boundaries are parameterized by their width and depth the results are expressed in a contour map, shown in Fig. 3.1. Although it may appear to be

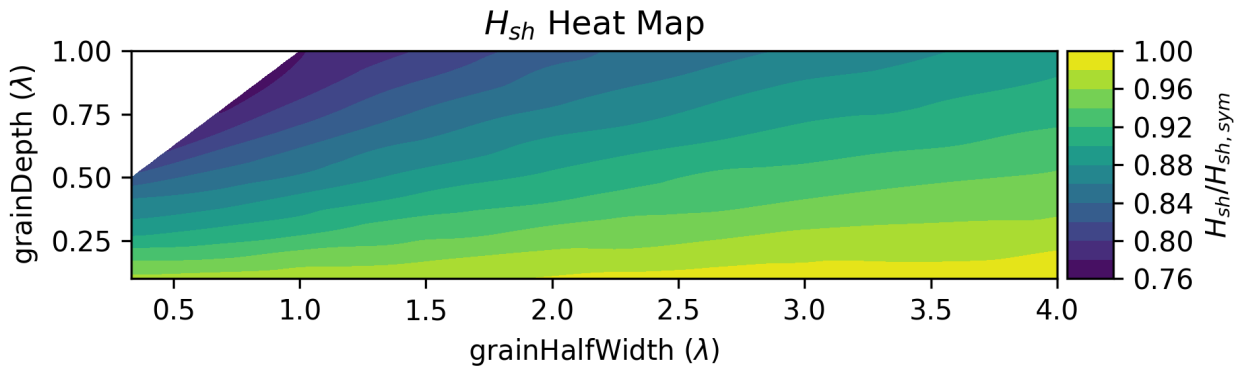

Figure 3.1 The percent decrease from an ideal geometry, expressed as $H_{\text{sh}}/H_{\text{sh.sym}}$, depends both on the depth and width of the grain boundary. High depth and low width values are excluded due to the inaccuracy in their calculation.

dependent on only the angle, an analysis shows that this is not the case, see Fig. 3.2. As shown, the reduction in H_{sh} is dependent on both the grain's depth and width. Values with very low widths and large depths were not able to be accurately calculated and were excluded from the figure.

The parameter used to generate the results for Fig. 3.1 is $\kappa = 4$, which was chosen because the computational costs were lower. Although this does not correspond to Nb or Nb3Sn—which are $\kappa = 2.3$ and $\kappa = 22.6$ respectively—similar trends in H_{sh} are expected in any type-II superconductor($\kappa \geq \frac{1}{\sqrt{2}}$). Thus the trends in our results should be valid for any value of κ.

Along with geometric deformities at grain boundaries, the inhomogeneities due to Sn segregation were found to negatively affect H_{sh}. As shown in Fig. 3.3, the introduction of inhomogeneities, modeled as a reduction from 1 in α, produces a near linear reduction on H_{sh}. The transition from an array of vortices entering in at once(as shown in Fig. 2.3b) to vortices first beginning to enter in the area where the inhomogeneity is present (see 2.5b) happens with $\alpha \leq 1 - 10^{-10}$. This means that nearly any degree of local imperfections lowers H_{sh}. Vortices penetrating at the boundary defects are theorized to spread out and eventually fill the bulk [2].

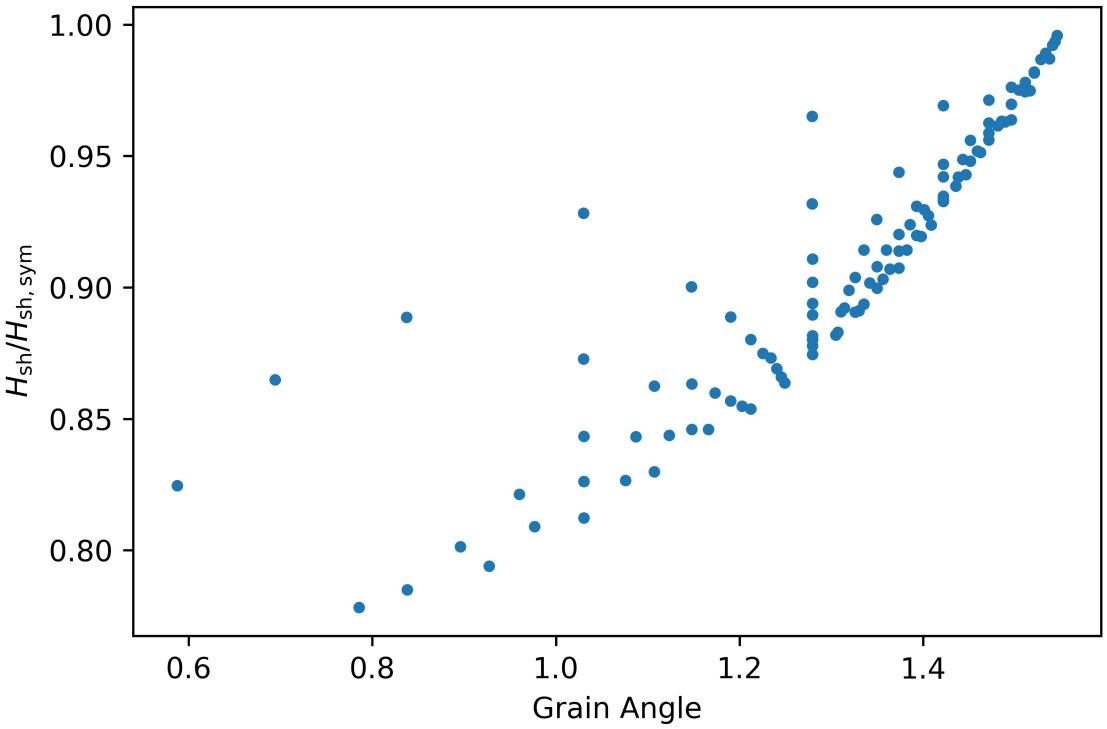

Figure 3.2 The fractional decrease from the superheating field (H_{sh}) of a symmetric mesh to one with a grain boundary geometry. The angle (in radians) is calculated by the arctangent of the half-width divided by the depth of the grain. This shows that H_{sh} is not dependent on the grain boundaries angle alone.

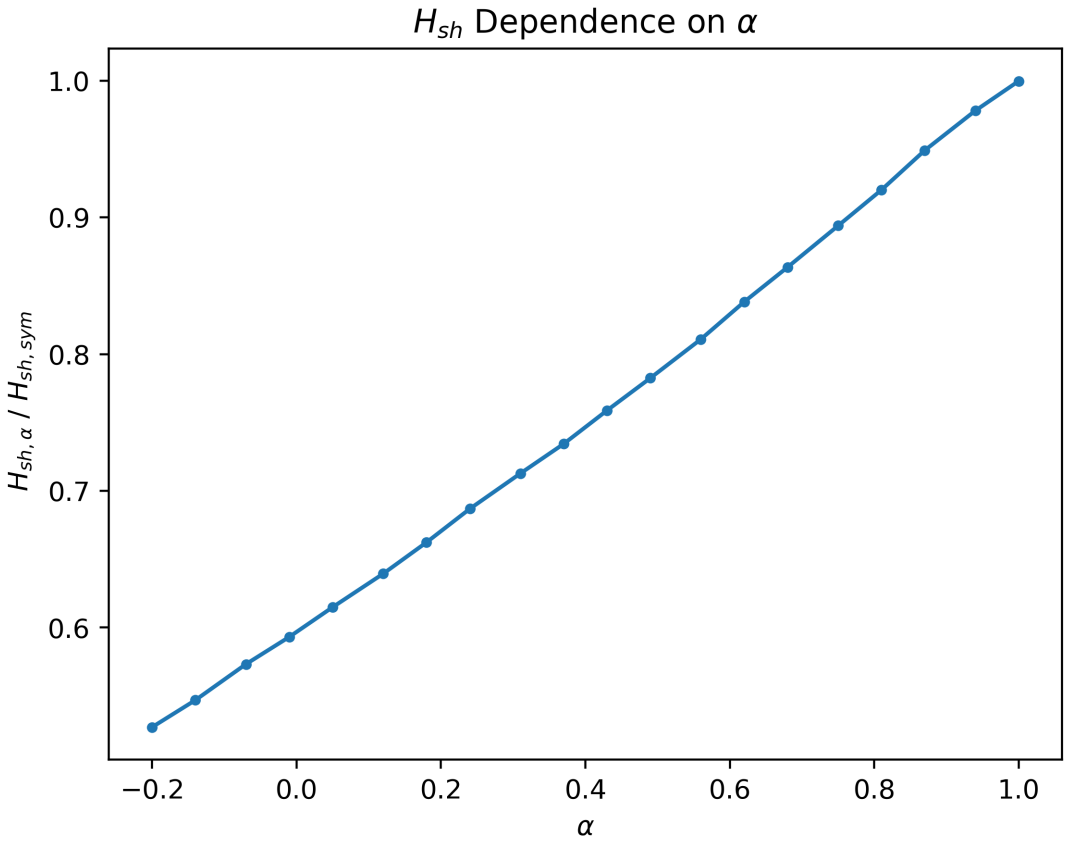

Figure 3.3 An increase in inhomogeneities—which corresponds to a reduction in α from 1—causes a near linear decrease in H_{sh}. The vertical axis shows the fractional reduction of H_{sh} from a perfectly symmetric case with no material inhomogeneities.

3.2 Conclusions and Future Work

The result from our simulation for a symmetric mesh agree with the theoretical predictions and thus confirm the accuracy of our simulations. Results from introducing geometric deformities and material inhomogeneities, which are present at grain boundaries, predict a significant lowering of H_{sh}. The implications for RFS cavity production reaffirms the need for smooth defect-free cavities. Although the combination of material geometric defects and inhomogeneities was not studied in detail, it is assumed that their combination would lower H_{sh} below the values calculated for either case independently, *e.g.* with the introduction of material inhomogeneities for a given geometric deformation H_{sh} would lower from when there is just a geometric deformation.

The software developed for these calculations can now be used to estimate H_{sh} for specifics materials—a known κ—with a known grain boundary characteristics. Due to the size and complexity of the code it is not included in this thesis but can be found at bitbucket.org/apack/ginzburg-landau-finite-element-scripts.git.

Improvements to the software would allow for the following phenomena to be studied. Vortex behavior inside a superconductor(including pinning sites and flux expulsion when cooling). This could be done by increasing mesh density within the bulk and would allow for an understanding of how heat is dissipated due to vortex nucleation. Field enhancements due to imperfections. This could be accomplished by having mesh elements outside the edge of the superconducting portion of the mesh. Finally, the effects of islands of inhomogeneities within a superconductor. By allowing alpha to take the form of different geometries within the mesh, studying this would help us understand how pockets of excess Sn within the bulk affect the H_{sh}. Further work should focus on these improvements.

Bibliography

[1] A. Gurevich, "Theory of RF superconductivity for resonant cavities," Superconductor Science & Technology **30,** 034004 (2017), pT: J; NR: 211; TC: 6; J9: SUPERCOND SCI TECH; PG: 25; GA: EL4ML; UT: WOS:000394595200001.

[2] M. K. Transtrum, G. Catelani, and J. P. Sethna, "Superheating field of superconductors within Ginzburg-Landau theory," Physical Review B **83,** 094505 (2011), pT: J; NR: 18; TC: 20; J9: PHYS REV B; PG: 8; GA: 730BF; UT: WOS:000288003000008.

[3] I. Dhiman, R. Ziesche, V. K. Anand, L. Riik, G. Song, A. T. M. N. Islam, I. Tanaka, and W. Treimer, "Thermodynamics of Meissner effect and flux pinning behavior in the bulk of single-crystal La2-xSrxCuO4 (x=0.09)," Physical Review B **96,** 104517 (2017), pT: J; NR: 85; TC: 0; J9: PHYS REV B; PG: 10; GA: FI4XI; UT: WOS:000411982600008.

[4] M. Tinkham, *Introduction to superconductivity* (McGraw-Hill, New York, 1975), Chap. 1-4.

[5] C. Becker, S. Posen, N. Groll, R. Cook, C. M. SchlepÃijtz, D. L. Hall, M. Liepe, M. Pellin, J. Zasadzinski, and T. Proslier, "Analysis of Nb3Sn surface layers for superconducting radio frequency cavity applications," Applied Physics Letters **106,** 082602 (2015), doi: 10.1063/1.4913617; 30.

[6] Y. Trenikhina, S. Posen, A. Romanenko, M. Sardela, J.-M. Zuo, D. L. Hall, and M. Liepe, "Performance-defining properties of Nb3Sn coating in SRF cavities," Superconductor Science and Technology **31,** 015004 (2017).

[7] V. L. Ginzburg, "Superconductivity and superfluidity (what was done and what was not)," Physics-Uspekhi **40,** 407–432 (1997).

[8] B. Li and Z. Zhang, "A new approach for numerical simulation of the time-dependent Ginzburg-Landau equations,", 2015, iD: 272570.

[9] A. Pack, Ph.D. thesis, 2017.

[10] M. Transtrum, Ph.D. thesis, 2011.

Index